

# 2023 | 362

## Characterization of future fuels using an optically accessible rapid compression machine

Basic Research & Advanced Engineering - Visualizations

Gerhard Pirker, LEC GmbH

Marc Klawitter, Graz University of Technology

Aravind Ramachandran, Graz University of Technology

Clemens Gößnitzer, LEC GmbH

Anton Tilz, LEC GmbH

Andreas Wimmer, LEC GmbH / Graz University of Technology

---

This paper has been presented and published at the 30th CIMAC World Congress 2023 in Busan, Korea. The CIMAC Congress is held every three years, each time in a different member country. The Congress program centres around the presentation of Technical Papers on engine research and development, application engineering on the original equipment side and engine operation and maintenance on the end-user side. The themes of the 2023 event included Digitalization & Connectivity for different applications, System Integration & Hybridization, Electrification & Fuel Cells Development, Emission Reduction Technologies, Conventional and New Fuels, Dual Fuel Engines, Lubricants, Product Development of Gas and Diesel Engines, Components & Tribology, Turbochargers, Controls & Automation, Engine Thermodynamics, Simulation Technologies as well as Basic Research & Advanced Engineering. The copyright of this paper is with CIMAC. For further information please visit <https://www.cimac.com>.

## ABSTRACT

Due to increasingly stringent environmental regulations in the field of energy and transportation systems, future fuels such as ammonia or hydrogen from renewable sources are promising solutions for internal combustion engines in various applications. The design of modern combustion systems for these fuels relies on advanced models and simulation tools which often require ignition, combustion and knocking properties as input, e.g., laminar burning velocity or minimum ignition energy, which are highly different from conventional fuels. To avoid expensive investigations directly at the engine test bed, fundamental investigations on special test rigs are the key to acquiring the important parameters that describe the combustion behavior of these fuels at relevant engine-like conditions.

This paper presents the results of fundamental investigations to gain insight into different characteristics of the combustion of future fuels within mixtures relevant to large engines. To this end, two different optical techniques are implemented on a rapid compression machine (RCM): Schlieren imaging to visualize the propagating spherical flame front in the optically accessible combustion chamber and Particle Image Velocimetry (PIV) for flow field measurements in a prechamber. Schlieren imaging is applied to investigate the laminar flame characteristics of  $\text{NH}_3/\text{H}_2/\text{N}_2/\text{air}$  flames at various cracking ratios, equivalence ratios and initial pressures. Specially designed spark plug electrodes are employed to minimize the influence of the ignition system hardware on the flame front shape. The PIV investigations use a prototype prechamber of production size that is large enough to allow optical access. Time-resolved planar velocity fields are obtained with which the nature of the flow in the prechamber is examined over the duration of the compression stroke using phase-invariant mean velocity fields. The scope of this study includes illustrating the implementation of PIV technique in the prechamber and presenting results obtained from the application of the measurement technique. These fundamental experiments represent an important building block in the overall development methodology of large engines that run on future fuels.

# 1 INTRODUCTION

## 1.1 Background and motivation

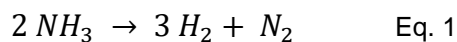
To reduce anthropogenic greenhouse gas emissions and thus the fatal effect on the world's climate, renewable energy must be employed in the form of carbon-neutral or carbon-free energy carriers and fuels. According to the latest IPCC Climate Change Mitigation Report, hydrogen and ammonia produced from renewable energy are promising candidates for the large engines sector [1]. Before these fuels can be used in internal combustion engines, their combustion behavior needs to be investigated thoroughly.

Despite its drawbacks in terms of combustion behavior, ammonia offers some advantages over hydrogen as a carbon-free energy carrier. It can easily be stored liquefied at ambient temperature and a pressure of less than 10 bar, or ambient pressure and a temperature of  $-33\text{ }^{\circ}\text{C}$ . Furthermore, the cost of storing ammonia can be as low as 1/30 of the cost of hydrogen [2]. In addition, infrastructure for the international transportation of ammonia already exists. However, the poor combustion behavior of ammonia (low laminar burning velocity, high ignition energy, narrow flammability limits, etc.) limits the use of pure ammonia as a fuel for practical applications.

One possible solution is to use hydrogen as a combustion promoter in combination with ammonia because it combusts much more intensely. By admixing the right share of hydrogen to ammonia, engine combustion in a fossil fuel-like manner is enabled. To avoid the need to store a second fuel, the required amount of hydrogen can be produced directly from ammonia by dissociation, so-called 'cracking' [3]. Design of an efficient combustion system for these alternative fuels (i.e., ammonia and hydrogen) requires detailed knowledge of their characteristics (e.g., laminar burning velocity, turbulent burning velocity) as well as the interaction between the flame and the flow field in the combustion chamber (e.g., turbulence). These parameters are also essential to the simulation and the design of the engine and must be determined in advance through fundamental investigations.

## 1.2 Fundamentals

The underlying reaction equation of ammonia cracking is given in Eq. 1 [3]. Nitrogen is produced as a byproduct.



In this context, the dissociation degree of  $\text{NH}_3$  is referred to as cracking ratio  $\gamma$ . It defines the fraction

of the original moles of  $\text{NH}_3$  that have been cracked into  $\text{H}_2$  and  $\text{N}_2$ . The cracking ratio  $\gamma$  of a given mixture is calculated by Eq. 2. The volumetric fractions of the fuel components at different cracking ratios are given in Table 1.

$$\gamma = \frac{x_{\text{H}_2}}{3/2 * x_{\text{NH}_3} + x_{\text{H}_2}} \quad \text{Eq. 2}$$

Since this paper does not focus on the actual cracking process, the required gas mixtures that represent the products of the cracking process are created for the present investigations by mixing pure gases on a gas mixing panel.

Table 1. Volumetric fractions of fuel components at different cracking ratios

Cracking ratio $\gamma$ / %	Vol. fraction $\text{NH}_3$ / %	Vol. fraction $\text{H}_2$ / %	Vol. fraction $\text{N}_2$ / %
0	100	0	0
10	81.82	13.64	4.55
20	66.67	25.00	8.33
40	42.86	42.86	14.29

The laminar burning velocity  $S_{L,u}^0$  (LBV, also laminar flame speed) is defined as the speed of an adiabatic unstretched premixed planar flame relative to the unburned mixture [4]. It is a key intrinsic property of combustible mixtures. The LBV is a decisive parameter for efficiency and stability in combustion optimization. The Markstein length  $L_b$  is a measure of the effect of curvature on the flame speed. These parameters are fundamental to simulations of combustion behavior as well as any estimation of performance in certain applications. Future fuels may fundamentally differ from conventional fuels in their combustion characteristics and fundamental parameters.

With spherically propagating flames, two methods can be implemented to derive the LBV and  $L_b$ . If flames have small radii on the scale of  $r_f = 10$  to 20 mm and exhibit a negligible rise in pressure, the constant pressure method is applied. Assuming constant pressure, the burned gas is quiescent and the flame speed relative to the burned gas can be directly calculated from the flame radius over time, which is gathered from optical data. In the case of larger flames with a considerable flame radius, the constant volume method is applied and the laminar burning velocity is derived from the pressure trace [5]. The investigations described in the present study only apply the constant pressure method. Spherically propagating flames can be subject to instabilities that cause wrinkling of the flame front. Apart from hydrodynamic instabilities, which are caused by density jumps in a moving flame front,

thermodiffusive instabilities may occur due to differential diffusion of heat and mass.

### 1.3 State of the art

In recent years, several publications have presented experimental results regarding the laminar burning velocity of  $\text{NH}_3/\text{air}$  flames [6–9] and  $\text{NH}_3/\text{H}_2/\text{air}$  flames [10–18]. To the best of the authors' knowledge, just four papers on experimental investigations of the laminar burning velocity of  $\text{NH}_3/\text{H}_2/\text{N}_2/\text{air}$  flames [19–22] are available. Mei et al. [19] and Ji et al. [20] apply the outwardly propagating spherical flame method, while Han et al. [21] use the heat flux method and Lesmana et al. [22] employ the vertical tube flame propagation method for low dissociation degrees and the Bunsen burner method for high dissociation degrees. In addition, Goldmann and Dinkelacker [23] have developed an approximation for the laminar burning velocity of  $\text{NH}_3/\text{H}_2/\text{N}_2/\text{air}$  flames based on a detailed reaction mechanism of Mathieu and Petersen [24] and experimental data available in the literature. While it has been reported that a laminar burning velocity close to the one of methane may be reached with a cracking ratio of  $\gamma = 40\%$ , engine applications indicate that lower cracking ratios are necessary for satisfactory operation, sometimes even below  $\gamma = 10\%$  [3, 25–29]. Most results have been published within the last five years, which reflects the rapidly increasing interest in practical applications of ammonia combustion systems and the required fundamental characteristics. Therefore, experimental and simulative investigations of future fuels need to be performed and established assumptions derived from conventional fuels have to be re-assessed. For instance, the assumption of a unity Lewis number for fuel-air mixtures – as with  $\text{CH}_4$  – is invalid for ammonia. Due to the change in combustion characteristics, the effect of boundary conditions such as flow and turbulence fields on combustion behavior varies [30, 31].

In flow field investigations of large engines, recent studies have indicated the need for detailed information on the flow field and mixing, especially in prechambers. In an optical investigation of prechamber combustion in a rapid compression expansion machine, Kotzagianni et al. [32] combined  $\text{OH}^*$  chemiluminescence imaging of prechamber-ejected flame jets in the main chamber with pressure measurements and computational fluid dynamics (CFD)-generated heat release rates. They studied the influence of varying the prechamber spark ignition timing on the subsequent combustion in the main chamber and noted that main chamber combustion after ignition by the prechamber jets could be relatively delayed and slow if the ignition timing were either too early or too late. This indicates an opportunity to address

a gap in knowledge if mixture formation and turbulence intensities in the prechamber can be measured in a time-resolved manner. This would yield the optimum injection and ignition timing for scavenged prechamber operation. Wellander et al. [33] performed fuel tracer planar laser-induced fluorescence (PLIF) measurements in a large bore natural gas optical engine and observed a significant amount of unburned gas ejected through the prechamber nozzles. This suggested that the gas mixing in the prechamber was incomplete and indicated the need for measurements of the processes that occur within the prechamber. While information regarding the flow field, mixture formation, ignition and subsequent combustion in prechambers is desired for an improved understanding of turbulent jet ignition, the small size of prechambers along with their geometry and installation render them impractical and unfeasible for optical investigations. While it is possible to scale up the dimensions of a prechamber for optical investigations, this has only been done with simplified prechamber and main chamber geometries [34, 35] or in a constant volume chamber with no charge motion [36].

### 1.4 Scope of the presented investigations

The investigations implemented two optical techniques separately on a rapid compression machine to gain insight into different characteristics of the combustion of future fuels within components relevant to large engines. Schlieren imaging of the laminar flame front was performed to capture its characteristics, and particle image velocimetry (PIV) investigations were conducted in a prechamber to capture the fundamentals of the flow field to which the flame front is exposed.

Applying Schlieren imaging, the laminar flame characteristics of  $\text{NH}_3/\text{H}_2/\text{N}_2/\text{air}$  flames are investigated for cracking ratios of  $\gamma = [10\%–40\%]$ , equivalence ratios of  $\phi = [0.7–1.3]$  and initial conditions of  $p_0 = [1 \text{ bar}–10 \text{ bar}]$  and  $T_0 = 298 \text{ K}$ . The limitations of the rapid compression machine in evaluation of laminar burning velocities are assessed.

The PIV investigations use a prototype prechamber of production size that is large enough to allow optical access. Time-resolved planar velocity fields are obtained to examine the nature of the fluid flow in the prechamber over the duration of the compression stroke using instantaneous and phase-invariant mean velocity fields. The scope of the present investigations includes illustration of the implementation of PIV technique in the prechamber and presentation of results obtained from the application of the measurement technique.

## 2 METHODOLOGY

### 2.1 Rapid compression machine

The combustion characteristics of future fuels are studied on an optically accessible rapid compression machine (RCM). It has a bore of 84 mm and an adjustable stroke range of 120 mm to 250 mm. At the maximum stroke, the combustion chamber has a volume of 1.38 dm<sup>3</sup>. The main combustion chamber has three side windows with dimensions of 40 mm x 20 mm. The windows are distributed around the perimeter of the main chamber near the fire deck. Details on the present RCM are found in [37].

### 2.2 Laminar flame measurements

This study applies the constant pressure method to an outwardly propagating flame. To calculate the laminar burning velocity, the flame front propagation within a quiescent gas mixture has to be captured optically and evaluated. To determine laminar burning velocities on an RCM, the machine must be operated as a constant volume combustion chamber. Therefore, the piston is not shot from bottom dead center (BDC) to top dead center (TDC) of the combustion chamber but remains at BDC during the laminar flame experiments.

Precise determination of laminar burning velocity is generally challenging. For instance, literature data show deviations in LBV of up to 40% for CH<sub>4</sub>/air flames [38]. Performing those measurements on an RCM imposes special boundary conditions, which have to be evaluated in an assessment of the impact on the quality of the measurement results. The maximum observable flame radius from the electrode gap to the edge of the side windows is approximately  $r_{f,max} = 15$  mm. According to Burke et al. [39], the effect of the cylindrical confinement is negligible for flame radii less than 30% of the wall radius and achieves an accuracy within 3%. Consequently, the maximum flame radius for the evaluation needs to be further reduced to  $r_{f,max} = 12$  mm for the given combustion chamber. Flame propagation is also influenced by the cylinder head, because the electrode gap is approximately 10 mm away from the cylinder head. The strong influence of wall confinement on the flame speed above  $r_{f,max} = 12$  mm is confirmed by the measurement data and depicted in Figure 2.

Figure 1 shows the Schlieren setup, which consists of a light source (Storz XENON NOVA 300), a pinhole, a collimating lens, the test area within the RCM main chamber, a converging lens, a second pinhole/knife edge and a high-speed camera. The high-speed schlieren camera (Photron SA-X2, Tokina Makro Optik AT-X, fixed focal length 100 mm, aperture f/5.6.) is oriented orthogonally to the

chamber side windows. Images of flame propagation, the spark, and other related phenomena are captured with a frame rate of 80000 fps, a shutter time of 10.88  $\mu$ s, and a resolution of 256 x 448 pixels.

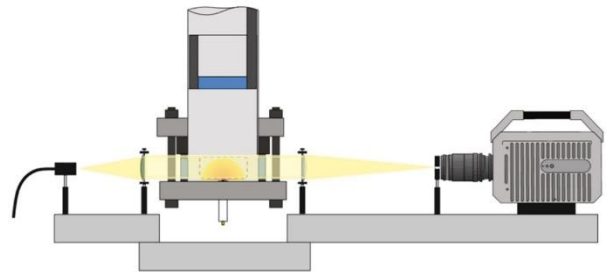


Figure 1. Scheme of Schlieren setup: lateral view in RCM main chamber

The optical measurement is complemented by temperature, pressure, spark voltage and current measurement. A fast high-range piezoelectric pressure sensor (Kistler 6045A) records the combustion pressure, and a low-range pressure sensor (Gems 3500) is used for the chamber filling process and the level adjustment of the fast pressure sensor. The gas temperature before combustion is confirmed by a thermocouple (K-Type) in the combustion chamber. The secondary voltage is measured at the spark plug connector cable with a high voltage clamp (Motortech SparcScan 1), and the secondary current with a 10:1 voltage probe (Yokogawa 7009-29). The measurement data are captured by an oscilloscope (Yokogawa DL850EV, 7012-50 measuring modules, 3 MHz bandwidth, 10 MS/s sampling rate, 12-bit resolution). Details on the measurement technology are found in [40].

For spark ignition, the gas mixtures are ignited by a modified large engine spark plug (Denso 301). To minimize the influence of the electrodes on the diffusion of radicals and heat transfer from the flame front, modified electrodes with a diameter of 0.5 mm are applied, see Figure 4. The spark gap is set to 0.4 mm. The ignition energy is delivered by a standard large engine control system. The ignition energy is set to the maximum with measured dissipated energies of 265–290 mJ.

The gas mixtures are created on a mixing panel by the partial pressure method. The pressure sensor (Keller PAA-33X) offers an accuracy of 0.05% FS. For homogenization and temperature equilibration, the mixtures rest in a mixing bottle for at least 30 minutes before the experiment. The used synthetic air consists of 80% nitrogen and 20% oxygen by volume. This low content of the oxidizer has to be considered when comparing the results to the literature data.

The optical raw data are postprocessed to extract the flame propagation. The original images are masked to the relevant area and a background image is subtracted to detect the contour of the flame front. The contour is analyzed and the flame radius is derived as a function of time in the region of the freely propagating flame. Only radii in the range of +/- 45° from the horizontal are averaged to one single radius, reducing the possible influence of buoyancy on slowly propagating flames and disturbances of the flame front by the spark plug electrodes, see Figure 4.

Assuming isobaric conditions for the evaluated range of flame radii, the burned flame speed equals  $S_b = dr/dt$ . A three-point stencil differentiation is applied to reduce the influence of noise on the accuracy of the subsequent extrapolation.

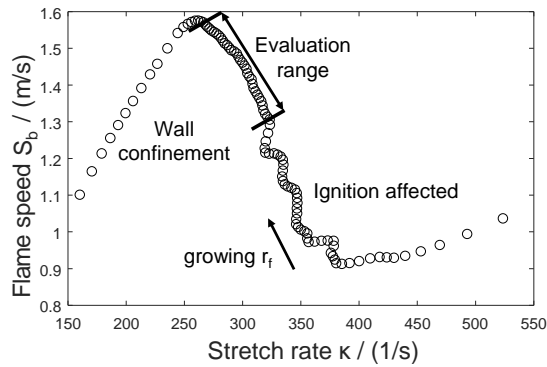


Figure 2. Flame speed  $S_b$  versus stretch rate  $\kappa$  of an  $\text{NH}_3/\text{H}_2/\text{N}_2/\text{air}$  flame;  $\gamma = 40\%$ ,  $\phi = 1.3$ ,  $p_0 = 1$  bar; evaluation range and areas affected by wall confinement and ignition

The unstretched burned flame speed  $S_b^0$  is calculated from  $S_b$  by extrapolation to zero stretch. For flames not strongly affected by stretch, e.g.,  $\text{CH}_4/\text{air}$  mixtures, linear extrapolation is reasonably adequate. This assumption cannot be transferred to  $\text{NH}_3/\text{H}_2/\text{N}_2/\text{air}$  flames [41]. Since the Lewis number of  $\text{NH}_3$  mixtures is different from unity, a nonlinear extrapolation needs to be applied. The chosen correlation is based on the stretched flame model of Ronney and Sivashinsky [42]. Assuming an adiabatic and quasi-steady flame, the relation is given by Eq. 3. Applying the extrapolation on the burned flame speed  $S_b$  yields the unstretched burned flame speed  $S_b^0$  and the Markstein length  $L_b$ , with respect to stretch rate  $\kappa$ . It is applied in its integrated form according to Kelley and Law [41] to directly fit the experimental data. This nonlinear extrapolation is implemented in all investigations on spherical propagating flames that are displayed in the results section [19, 20].

$$\left(\frac{S_b}{S_b^0}\right)^2 * \ln\left(\frac{S_b}{S_b^0}\right)^2 = -2 \frac{L_b * \kappa}{S_b^0} \quad \text{Eq. 3}$$

The lower and upper limits of the evaluation range considered for extrapolation are chosen based on the measurement conditions within  $R_{f,\min} = 6$  mm and  $R_{f,\max} = 12$  mm. The lower limit is influenced by ignition and flame curvature unsteadiness and is related to the Lewis number of the mixture, see [41, 43]. The upper limit is influenced by the confinement of the combustion chamber [38] as discussed above. For instance, the flame speed of an  $\text{NH}_3/\text{H}_2/\text{N}_2/\text{air}$  flame with  $\gamma = 40\%$  and  $\phi = 1.3$  at  $p_0 = 1$  bar shows a significant change in behavior at a stretch rate below  $270 \text{ s}^{-1}$ , which corresponds to  $r_f = 11.5$  mm, see Figure 2. In contrast, Mei et al. [19] evaluate flame radii from 10 to 23 mm, and Ji et al. [20] evaluate between 8–12 to 20 mm. Further literature suggests a lower limit of 10 mm, which is not applicable in the present investigations due to the early confinement on the RCM.

$$S_u^0 = \rho_b / \rho_u * S_b^0 \quad \text{Eq. 4}$$

Applying the principle of mass conservation, the unburned, unstretched flame speed  $S_u^0$  is to be derived by  $S_b^0$ , and the density ratio of burned to unburned gas, Eq. 4. The densities are calculated using an equilibrium calculation in Cantera [44] and a reaction mechanism by Konnov [45]. Finally, the unburned, unstretched flame speed  $S_u^0$  is equivalent to the laminar burning velocity.

Table 2. Laminar flame experiment parameters

Parameter	Value
RCM main chamber volume / $\text{dm}^3$	1.38
RCM bore / mm	84
Window dimension / mm	40 x 20
Maximum flame radius evaluation range / mm	6 - 12
Dissipated energy ignition system / mJ	265 - 290

To ensure repeatability, every measurement point is measured at least three times. The average, minimum, and maximum value of the valid repetitions are presented in the results. Before every iteration, the chamber is scavenged and evacuated to remove residual combustion products. After every iteration at  $p_0 = 5$  bar or  $p_0 = 10$  bar, the combustion chamber is opened and cleaned to remove condensed water from the chamber walls and the spark plug. The lower cracking ratio is limited by the ignitability of the gas mixtures with the given industrial ignition system.

### 2.3 Flow field measurements

Velocity measurements using PIV were performed in a prototype prechamber with eight nozzles and a neck with an inclination of  $7^\circ$ . The prechamber had a total volume of  $33 \text{ cm}^3$ , which is comparable to the prechambers of large gas engines and is 22%

of the RCM main combustion chamber volume at TDC. The ratio of the total cross-sectional area of the prechamber nozzles to the volume of the prechamber ( $A/V$  ratio) is  $0.023 \text{ cm}^{-1}$ . An inclined neck as opposed to a symmetric and straight neck prechamber geometry was chosen to impose a fixed direction on incoming flow into the prechamber bottle. Furthermore, it was chosen to minimize out-of-plane motion which cannot be captured by two-dimensional, two-component (2D2C) particle image velocimetry. For optical access, three windows were installed into the prechamber: two for entry and exit of the laser sheet, respectively, and one for camera access. The windows had a diameter of 16 mm, which was a limit determined by the small size of the prechamber.

The PIV setup consisted of a dual-head pulsed Litron LDY-304 Nd:YLF laser operating Q-switched at a repetition rate of 10 kHz and a Photron SA-X2 high-speed CMOS camera operating in double frame mode at 20 kHz to capture the Mie scattering from each of the laser pulses. The camera was operated at a resolution of  $768 \times 768$  pixels to achieve the desired recording frame rate, and it was fitted with a Tokina AT-X Pro 100 mm focal length macro lens with the aperture set at  $f/8$ . The frequency-doubled output of the Nd:YLF laser produced a 5 mm diameter beam of 527 nm wavelength. This beam was guided toward the prechamber through a light guide arm and then passed through sheet-forming optics (a converging spherical lens and a diverging cylindrical lens). The laser sheet thus formed was passed through the window into the prechamber, illuminating a planar section inside where the velocities would be measured, see Figure 3.

The principle of PIV involves acquiring a pair of images of seeding particles in the flow field at a predefined time separation and computing the displacement of the particles between the two acquired images. Thus velocities can be obtained from the measured displacements. The pulse separation was set to  $5 \mu\text{s}$  based on the velocities expected in the prechamber. Microscopic graphite particles of a mean diameter of  $3.5 \mu\text{m}$  were used for seeding, as graphite also functions as a lubricant for the machine and does not have a strong tendency to agglomerate. The seeder particles were injected into the main combustion chamber with a syringe and then mixed with the flow of air into the machine during the pre-shot gas filling stage. The amount of seeding had to be sufficient to be measurable during the initial stages of the shot while not being excessive during peak pressure.

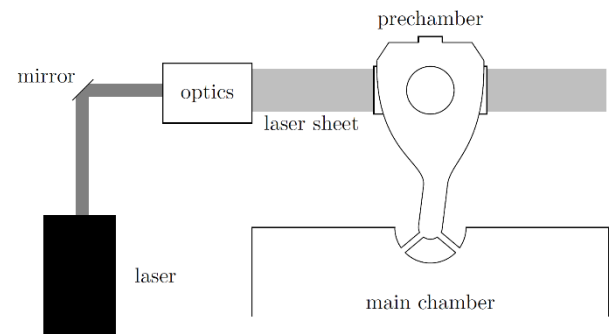


Figure 3. Dual head Nd:YLF laser (Litron LDY304) with the sheet forming optics and prechamber attached to the cylinder head of the rapid compression machine; top view from the laboratory frame of reference.

Compression shots were performed in the RCM with initial pressures of the driving and charge gas volumes set to result in a compression ratio of 10.0 during the shot. In the experiments reported here, the maximum allowable stroke of the RCM was set to 248 mm. Pressure in the main combustion chamber and pressure in the prechamber were measured by a Kistler 6045A piezoelectric pressure sensor and an AVL GH14D piezoelectric sensor, respectively. The relative pressure values from these two sensors were pegged to the initial charge pressure by using pressure values simultaneously measured in the main chamber by a GEMS 3100 series static pressure sensor. These pressure measurements were recorded along with the simultaneously measured piston position on a 10-channel Yokogawa DL850EV oscilloscope. Data was acquired by the oscilloscope at a rate of 1 million samples per second. This data acquisition was triggered at a piston position of 25 mm after BDC. The motion of the piston is captured by an RLS LM10 magnetic encoder. The peak main chamber pressure value in the shots lay between 41 and 42 bar, and the piston arrived at TDC at  $t = 0.0396 \text{ s}$ , where  $t = 0 \text{ s}$  refers to a piston position of 25 mm after BDC (the trigger point for data acquisition). PIV data obtained were processed using the open source PIV package OpenPIV [46] in Python. Each pair of particle scatter images was divided into  $64 \times 64$  pixel interrogation windows with 75% overlap and the velocities were computed in each interrogation window by a cross-correlation algorithm with multipass window deformation. The resulting vectors were then passed through validation stages, including range validation, peak validation, local median validation and finally outlier removal and smoothing using the method developed by Garcia [47]. The vector fields were then rearranged into phase-locked ensembles, i.e., ensembles of velocity fields at each time step across the shots. All postprocessing was performed using in-house Python codes.

Table 3. Flow field experiment parameters

Parameter	Value
RCM maximum allowable stroke / mm	248
RCM bore / mm	84
Compression ratio / -	10.0
Prechamber volume / cm <sup>3</sup>	33
Prechamber nozzle diameter / mm	3.5
Number of prechamber nozzles / -	8
Prechamber nozzle area to volume ratio / cm <sup>-1</sup>	0.023
Prechamber neck angle of inclination/ °	7
Laser pulse separation / μs	5

### 3 RESULTS AND DISCUSSION

The aim of the results and discussion section is to increase understanding of the combustion characteristics of future fuels in large engines as well as provide valuable data for creating and validating simulation models. First, the available data on laminar flame characteristics of NH<sub>3</sub>/H<sub>2</sub>/N<sub>2</sub>/air mixtures is supplemented and the quality of measurements of the laminar burning velocity on an RCM is assessed. Second, the flow field in a production-sized large engine prechamber is assessed. These two fundamental investigations will serve as the baseline for future investigations in which models are created and calibrated in order to calculate the flame propagation of these novel fuels in real engines.

#### 3.1 Schlieren imaging results

Table 4 provides the test conditions of the experiments on NH<sub>3</sub>/H<sub>2</sub>/N<sub>2</sub>/air flames. The initial temperature is set to T<sub>0</sub> = 298 K ± 3 K. Figure 4 presents Schlieren images of the NH<sub>3</sub>/H<sub>2</sub>/N<sub>2</sub>/air flames at different pressures, cracking ratios and equivalence ratios. The outwardly propagating flames are ignited in the visible electrode gap and propagate from there. All flames are presented at a flame radius of approximately r<sub>f</sub> = 10 mm, which lies within the evaluation range for the laminar burning velocity. Due to the different flame speeds of the mixtures, the snapshots shown in Figure 4 were all taken at different times after ignition to obtain approximately the same flame radius.

Table 4. Test conditions for NH<sub>3</sub>/H<sub>2</sub>/N<sub>2</sub>/air mixtures, initial temperature T<sub>0</sub> = 298 K

Cracking ratio γ / %	Initial pressure p <sub>0</sub> / bar	Equivalence ratio φ / -
40	1, 2, 5, 10	0.7 – 1.3; Δ = 0.1
20	1, 2, 5	1.0
10	1, 2, 5	1.0

In the high-pressure cases, the flame front appears darker because of the larger density gradient between the burned and unburned zones. The buoyancy effect is largest in the slowest propagating flames at a cracking ratio of γ = 10%. In addition, the flame front is visibly disturbed by the fine electrodes in the vertical direction. As described in the methodology section, these effects are considered by evaluating the flame front in the range of +/- 45° to the horizontal axis. The visible electrode gap difference of single measurements has no quantifiable influence on flame propagation in the evaluated range.

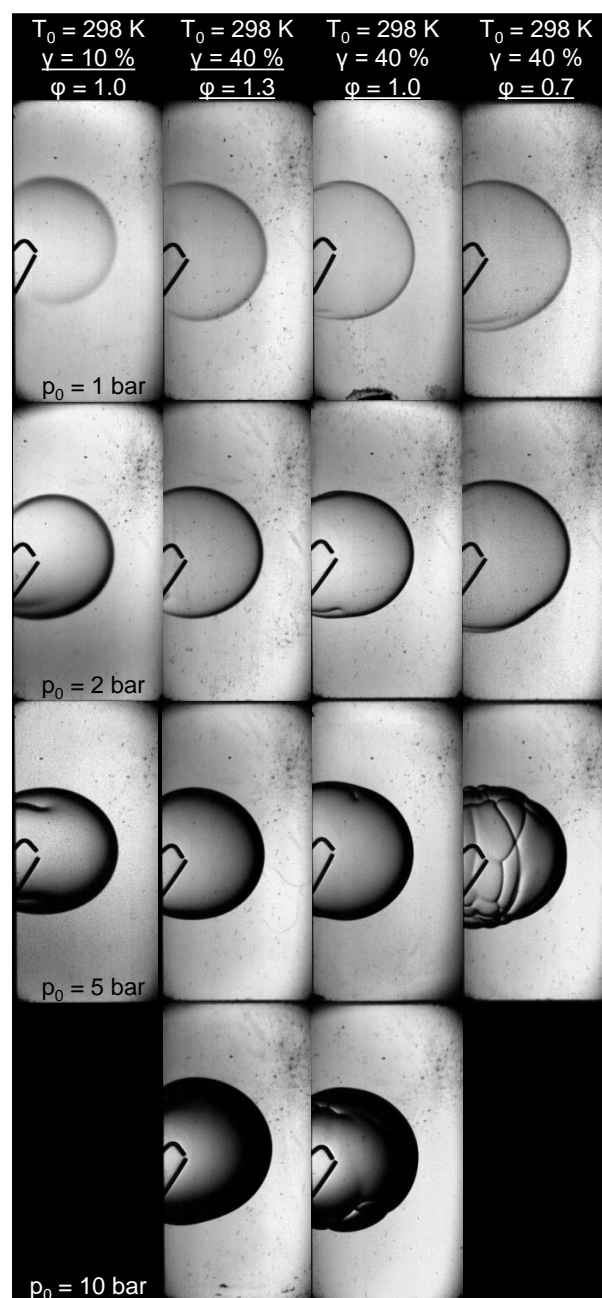


Figure 4. Schlieren images of NH<sub>3</sub>/H<sub>2</sub>/N<sub>2</sub>/air flames at a flame radius of r<sub>f</sub> = 10 mm, different pressures, cracking ratios and equivalence ratios and T<sub>0</sub> = 298 K

Applying the described evaluation method yields the results for the laminar burning velocity and Markstein length. The range of evaluable boundary conditions for the laminar burning velocity is further limited by instabilities on the flame front surface. While hydrodynamic instabilities affect all moving flame fronts, especially gas mixtures with a Lewis number below unity are sensitive to thermodiffusive instabilities [48]. Increasing the cracking ratio, increasing the pressure and decreasing the equivalence ratio favor instabilities. Instabilities cause the formation of cellular structures on the flame front surface. The increased surface area results in an increased flame propagation speed. The onset of such instabilities is visible in Figure 4 for  $T_0 = 298$  K,  $\gamma = 40\%$ ,  $\phi = 0.7$ , and  $p_0 = 5$  bar.

When  $T_0 = 298$  K,  $\gamma = 40\%$ , and  $p_0 = 10$  bar, the  $\phi = 1.0$  flame is considered stable within the evaluation range of  $r_f \leq 12$  mm, see Figure 4. Decreasing the equivalence ratio to slightly lean conditions of  $\phi = 0.9$ , the flame becomes unstable below  $r_f = 12$  mm, see Figure 5. Therefore, the LBV of the  $\phi = 0.9$  flames cannot be calculated. At a flame radius above  $r_f = 15$  mm, the cellular structures are already very pronounced. The present findings follow the considerations of Bechtold and Matalon, according to which a critical radius for the onset of thermodiffusive instabilities must be reached [48].

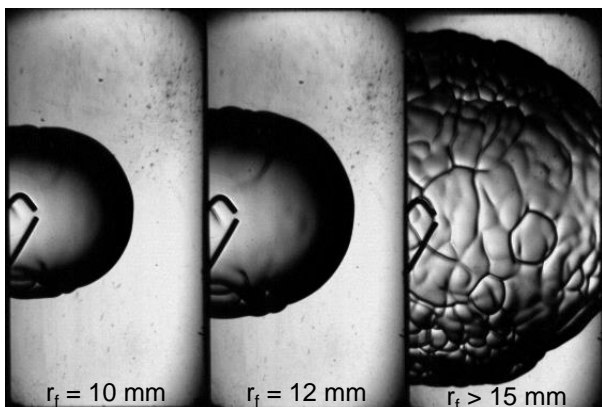


Figure 5: Schlieren images of  $\text{NH}_3/\text{H}_2/\text{N}_2/\text{air}$  flame at different radii,  $\gamma = 40\%$ ,  $\phi = 0.9$ , and  $p_0 = 5$  bar; onset of instabilities visible

### 3.2 Laminar flame propagation of $\text{NH}_3/\text{H}_2/\text{N}_2/\text{air}$ mixtures

The dependency of the LBV of  $\text{NH}_3/\text{H}_2/\text{N}_2/\text{air}$  flames on the equivalence ratio and pressure at  $T_0 = 298$  K and  $\gamma = 40\%$  is shown in Figure 6. The only available literature data concerning this cracking ratio are from Mei et al. [19]. Both datasets show a decrease in LBV with increasingly lean and rich mixtures, which is caused by higher dilution in lean mixtures and incomplete combustion in rich mixtures. With rich mixtures, the deviations to Mei

are below 2 cm/s. The pressure effect for pressures up to 10 bar is almost identical with rich mixtures in both of these studies. The equivalence ratio effect on the LBV tends to decrease at higher pressures. Furthermore, the peak LBV does not shift at different pressure levels.

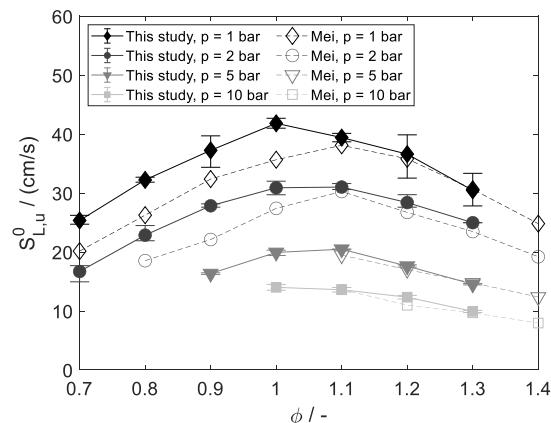


Figure 6. Laminar burning velocity of  $\text{NH}_3/\text{H}_2/\text{N}_2/\text{air}$  flames vs. equivalence ratio and pressure at  $T_0 = 298$  K, and  $\gamma = 40\%$ ; For the present data, the average, minimum, and maximum value are indicated; Mei et al. [19]

In Mei et al. [19], the LBV peaks for an equivalence ratio around  $\phi = 1.1$ . This agrees with the measurement data of Ji, which were measured at different cracking ratios and thus are not displayed [20]. A peak LBV at slightly rich conditions is also confirmed by reaction kinetic calculations with various reaction mechanisms [19–22]. In contrast, the present data peak around  $\phi = 1.0$  as part of a general discrepancy between it and the literature data at stoichiometric and lean conditions. While the present data at rich conditions agree with Mei, the data at  $\phi = 1.0$  and leaner conditions show deviations. This discrepancy is also visible in the results of the Markstein length, see Figure 7. The results of Mei for  $p_0 = 1$  bar drop to a Markstein length of around  $L_b = -3$  mm for  $\phi = 0.7$ . Gotama achieved comparable results for  $\text{NH}_3/\text{H}_2/\text{air}$  flames with a volumetric  $\text{H}_2$  fuel content of 40% ( $L_b = -2.7$  mm for  $\phi = 0.8$ ). In contrast, the present results yield a Markstein length close to zero at  $\phi = 0.7$ .

The discrepancies in both LBV and  $L_b$  are possibly caused by the narrow and comparatively low evaluation range in this study due to the geometrical limitations of the RCM. Under stoichiometric and lean conditions, it is assumed that the effect of stretch on flame propagation is not fully captured within the evaluation range, which leads to diverging extrapolation results. According to Eq. 3, a small absolute value of  $L_b$  indicates a small effect of stretch on LBV, which supports the assumption. This restriction has to be considered in an evaluation of the following results.

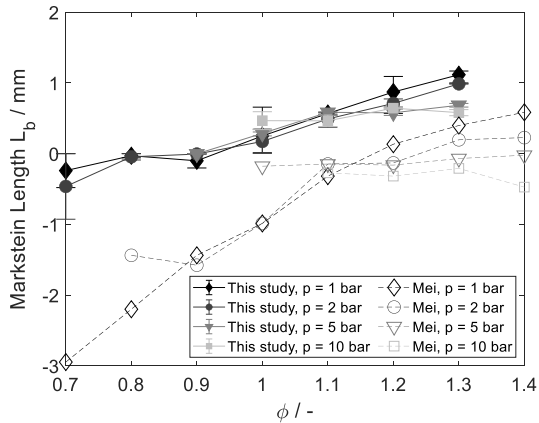


Figure 7. Markstein length of  $\text{NH}_3/\text{H}_2/\text{N}_2/\text{air}$  flames vs. equivalence ratio and pressure at  $T_0 = 298 \text{ K}$  and  $\gamma = 40\%$ ; For the present data, the average, minimum, and maximum value are indicated; Mei et al. [19]

As the equivalence ratio decreases and the pressure increases, the flame becomes more unstable, following the results of Mei. However, Mei starts to exclude measurement points due to the onset of instabilities in mixtures that are not as lean as those in the present results. As shown in Figure 4, the flames at  $p_0 = 2 \text{ bar}$  and  $\phi = 0.7$  and also at  $p_0 = 10 \text{ bar}$  and  $\phi = 1.0$  have a smooth surface and may therefore be evaluated. The results of Mei are more limited due to the larger evaluation range. While no instabilities are apparent for flame radii below  $r_f = 12 \text{ mm}$  in our study, the flame front may be subject to instabilities at radii up to  $r_f = 23 \text{ mm}$ , as considered by Mei et al. [19].

Figure 8 shows the present results compared to the literature data of the laminar burning velocity versus the cracking ratio of ammonia at  $p_0 = 1 \text{ bar}$ ,  $T_0 = 298 \text{ K}$ , and  $\phi = 1.0$ . The data of Ji et al. [20] and Lesmana et al. [22] are based on a different definition of the dissociation degree and are converted to the cracking ratio. Despite the aforementioned restrictions of the present data at stoichiometric conditions, they correctly capture the dependency of the LBV on the cracking ratio. Except for Lesmana [22], all results show good agreement between a nonlinear correlation of LBV and  $\gamma$ , while the results presented in this study and Ji's results yield noticeably higher LBV values than Mei and Han. In contrast, Lesmana's results are significantly lower than the broad literature agreement and suggest a decreasing effect on LBV as  $\gamma$  increases. These results are obtained using the Bunsen method. Bunsen method results have already been shown to underestimate the LBV compared to other methods [21]. Given the generally high discrepancies of flame speeds measured from outwardly propagating spherical flames [38], the results from this study fall well within the range of the literature results.

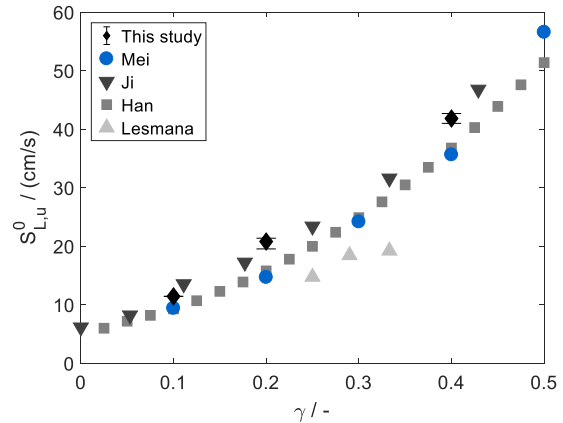


Figure 8. Laminar burning velocity of  $\text{NH}_3/\text{H}_2/\text{N}_2/\text{air}$  flames vs. cracking ratio at  $p_0 = 1 \text{ bar}$ ,  $T_0 = 298 \text{ K}$  and  $\phi = 1.0$ ; For the present data, the average, minimum, and maximum value are indicated; Mei et al. [19], Ji et al. [20], Han et al. [21], Lesmana et al. [22]

All literature data agree on a monotonically rising LBV as  $\gamma$  increases caused by the rising  $\text{H}_2$  content. While the  $\text{N}_2$  content also rises along with the cracking ratio, the negative influence of the additional inert gas on flame propagation is minor as shown by Mei et al. [19]. At a cracking ratio of  $\gamma = 40\%$ , all studies yield an LBV equal to or higher than the LBV of  $\text{CH}_4$  under the same conditions ( $S_{L,u}^0 = 36 \text{ cm/s}$ ).

Figure 9 presents the influence of pressure on LBV at several cracking ratios and  $T_0 = 298 \text{ K}$  and  $\phi = 1.0$ . The LBV decreases monotonically as the pressure increases. Already at comparatively low pressures of up to  $p_0 = 10 \text{ bar}$ , the LBV tends to approach a lower limit.

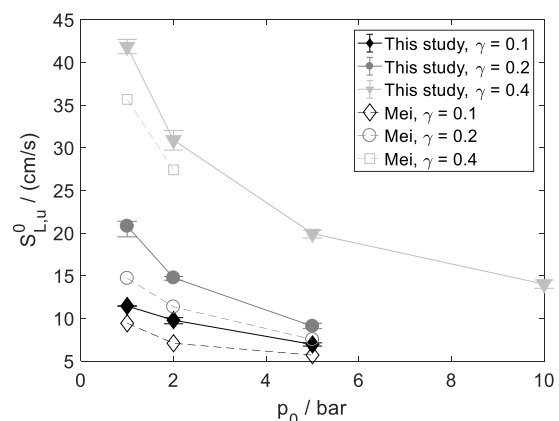


Figure 9. Laminar burning velocity of  $\text{NH}_3/\text{H}_2/\text{N}_2/\text{air}$  flames vs. initial pressure and cracking ratio at  $T_0 = 298 \text{ K}$  and  $\phi = 1.0$ ; For the present data, the average, minimum, and maximum value are indicated; Mei et al. [19]

At higher pressures and under engine-relevant conditions, the pressure effect on the LBV is expected to be minimal, as shown by Andrews and Bradley for CH<sub>4</sub>/air flames [49]. At all pressure levels, the results of the study presented here and Mei's results exhibit a similar increase in LBV over the rising cracking ratio [19]. At high cracking ratios, the pressure effect strongly intensifies. However, the study data yield higher LBV values due to the mentioned restrictions. While the absolute deviations of the data tend to decrease as pressure increases, the relative deviations remain in the same order of magnitude.

### 3.3 Flow velocity measurements in a prechamber

As mentioned above, the RCM setup had to be modified for the PIV measurements in the prechamber. In contrast to the fixed piston at BDC in the LBV measurements, the piston is shot from BDC to TDC in the PIV investigations. As the compression shot occurs, the rapid movement of the piston pushes gas (in this case air) from the main combustion chamber through the eight nozzles into the prechamber, where the air flows through the prechamber neck into the prechamber. PIV data became usable after around  $t = 0.015$  s after the start, when enough seeding particles enter the window as the flow enters the bottle region of the prechamber. Mean velocity fields at each time step were obtained by phase invariant averaging of the instant velocity fields across all the shots.

From the six mean flow field snapshots at different time instants shown in Figure 10, it can be seen that despite the limited field of view, it is possible to obtain a picture of the development of the flow field in the prechamber over the course of the rapid compression shot. The inclination of the neck guides this flow in the prescribed direction as can be seen from the flow field snapshot at  $t = 0.0259$  s in Figure 10(a). Shortly afterward at  $t = 0.0289$  s, Figure 10(b) shows this incoming flow moving towards the right-side edge of the window, indicating that the flow has begun to follow the inner wall of the prechamber more closely. As visible in the Figure 10(c) snapshot at  $t = 0.0318$  s, the flow is deflected laterally at the top wall of the bottle near the spark plug and oriented back towards the direction of the neck on the left side of the window; shortly thereafter it begins to interact with the incoming higher velocity flow through the neck. Following this interaction, a salient feature of the prechamber flow field is observed as the piston approaches TDC, namely a tumble vortex in the meridian plane. This tumble is seen to be convected through the field of view in the center of the prechamber bottle over a time span that includes periods of the shot both before and after

the piston arrives at TDC as shown in Figure 10(d-f). This feature appears consistently in the shots performed. Ultimately, the tumble collapses as the reverse pressure gradient between the prechamber and main chamber after TDC drives the flow back out of the prechamber. As the formation of the vortex was not directly observed, it is assumed that the vortex forms with its center outside the observable window and subsequently moves into the PIV field of view.

Tumble vortices are a common flow feature in combustion engines [50, 51] and are beneficial and desirable for increasing the residence time of the fuel and air in the engine and assisting in the formation of a reliably ignitable mixture in the combustion chamber at ignition time. The tumble flow structure is also capable of maintaining kinetic energy and dissipating it smoothly to smaller structures in the flow, leading to low turbulence intensities over the course of its lifetime. While main chamber charge homogeneity is less sensitive in the case of a jet ignition engine, an experimental study by Bunce et al. [52] in a jet-ignited gasoline engine found that an increased tumble in the main chamber charge led to a not insignificant increase in indicated and brake thermal efficiencies. In an engine cylinder, however, a tumble that is formed is typically broken down by the motion of the piston as it approaches TDC, and this breakdown dissipates turbulent kinetic energy close to the ignition time, contributing to faster propagation of the flame kernel formed by ignition. As the prechamber used in the present study is typically operated with spark ignition, such a tumble structure has a significant influence on the turbulence and mixture formation in the prechamber. It dictates the ignitability of the fluid in the immediate vicinity of the spark plug at the time of ignition and also has an impact on cycle-to-cycle variations. Therefore, the lifetime of the structure is also of great importance with respect to spark timing. As there is no piston in the prechamber, unlike the main combustion chamber, this tumble vortex cannot be squished by piston motion, but must be broken down by the turbulent flow field in the prechamber or when the flow is eventually driven back out of the prechamber with the reversal of the pressure gradient.

Tumble in the prechamber from the two-dimensional velocity field was identified and the motion of its center was tracked using the vortex identification method described by Graftieaux et al. [53]. This method subdivides the velocity field into several smaller areas and finds a point P in each subdivided area from which a radial vector PM drawn to any point M within the defined area is at a right angle to the velocity vector at point M.

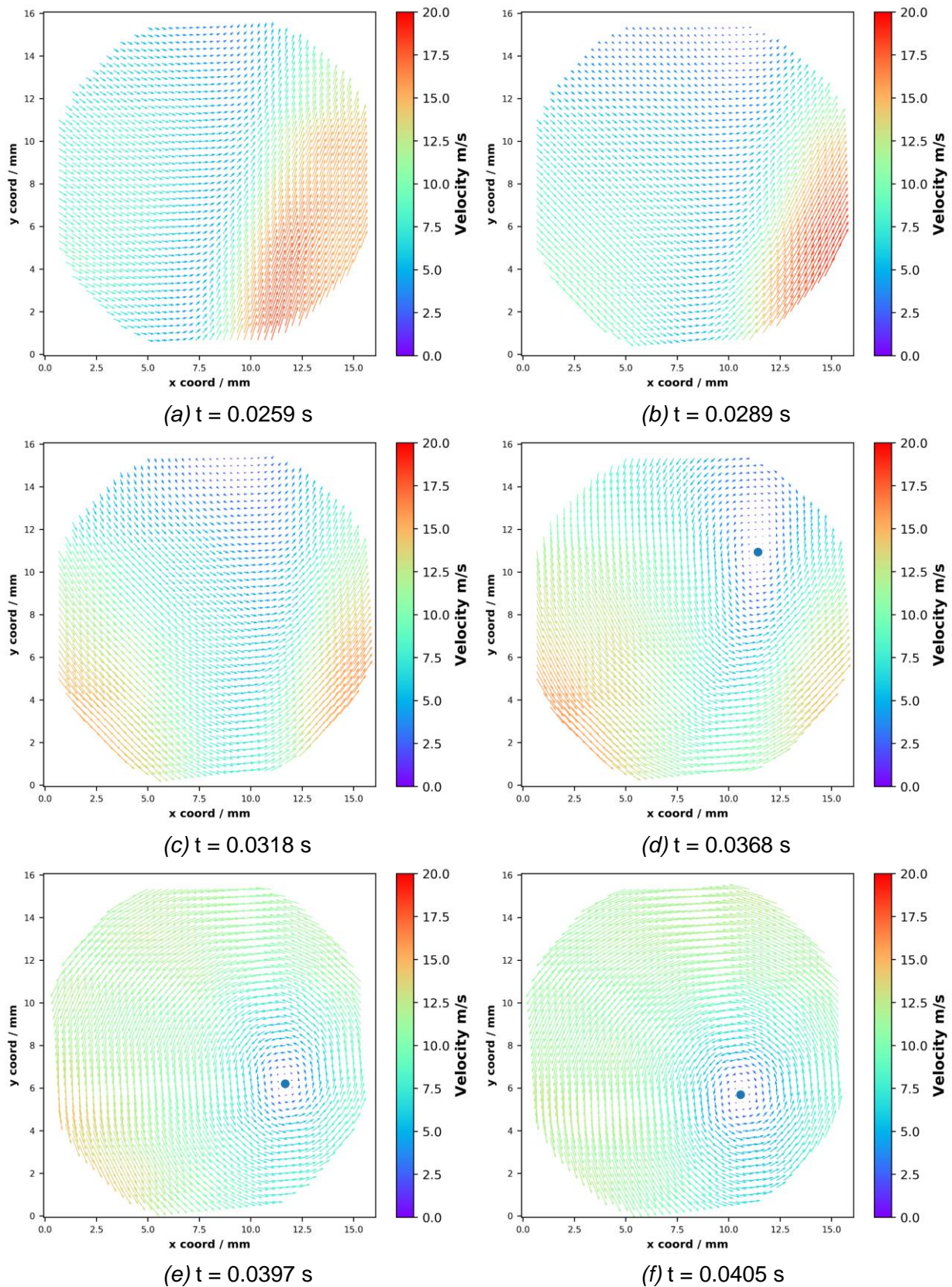


Figure 10. Sample mean flow field at several time instants with a dot representing the center of the identified tumble vortex. The beginning of data acquisition  $t = 0$  s refers to a piston position of 25 mm after BDC. Note that the field of view orientation is consistent with that of the prechamber window in Figure 3.

If such a point is found, it must therefore be the center of a vortex. The coordinates of the vortex center location are then marked as the tumble center at that instant. Sample velocity fields from the mean shot at different time instants are shown in Figure 10; a dot represents the tumble center location.

The shot-to-shot variability in the tumble path is analyzed by plotting two-dimensional joint probability distribution maps of the tumble center locations across all shots, see Figure 11. This joint probability distribution was evaluated over two time periods: one from 0.0360 s to 0.0395 s (3.6 ms duration leading up to TDC) and one from 0.0396 s to 0.0465 s (7 ms duration from TDC onwards). Splitting up the time duration into two segments – before TDC and after TDC – illustrates the difference in the spread of the tumble center location during these distinct periods in the compression stroke. The path of the tumble center in the mean shot was tracked over this 10.5 ms duration and has been overlaid on both probability distribution maps for the corresponding time ranges. Given that the duration of time analyzed in these maps in the pre-TDC period is half of the duration covered in the post-TDC period, it can be seen that the tumble center moves over a larger area in the window before TDC than after TDC. Thus, the tumble is convected across the window by the pre-TDC mean flow and exhibits significant variability in its center location owing to turbulence in the flow field. The post-TDC flow aligns the tumble center motion in a nearly 45° angle with respect to the prechamber axes, see Figure 11(b). In addition, the variability in tumble center locations is lower around the center of the window during this time period.

The influence that a rotational flow in the prechamber in the form of tumble can have on prechamber combustion and subsequent flame propagation was captured in the CFD simulations of Kirkpatrick et al. [54]. They simulated a prechamber-ignited large bore gas engine and showed the formation of a vortex inside the prechamber induced by the incoming flow from the main chamber that was very similar to the tumble observed in the measurements of this study. Crucially, the simulations showed that the flame propagation after ignition in the prechamber followed the direction of the rotating gas flow. While simultaneous flame imaging in the prechamber along with PIV acquisition is outside the scope of this study, combustion and flame propagation in the prechamber and the interaction of the ejected flame jets with the fuel-air mixture in the main chamber will be the subject of future investigations. Furthermore, as the mixing of fuel and air inside the prechamber is critical to successful ignition in the

prechamber and the subsequent ignition of the lean charge in the main combustion chamber, the nature of the turbulence in the prechamber must be understood. From the acquired PIV data, the velocity fluctuations in two directions can be computed and then used to calculate the turbulent kinetic energy, after which the impact of the turbulent flow field in this prechamber on combustion may be examined in detail.

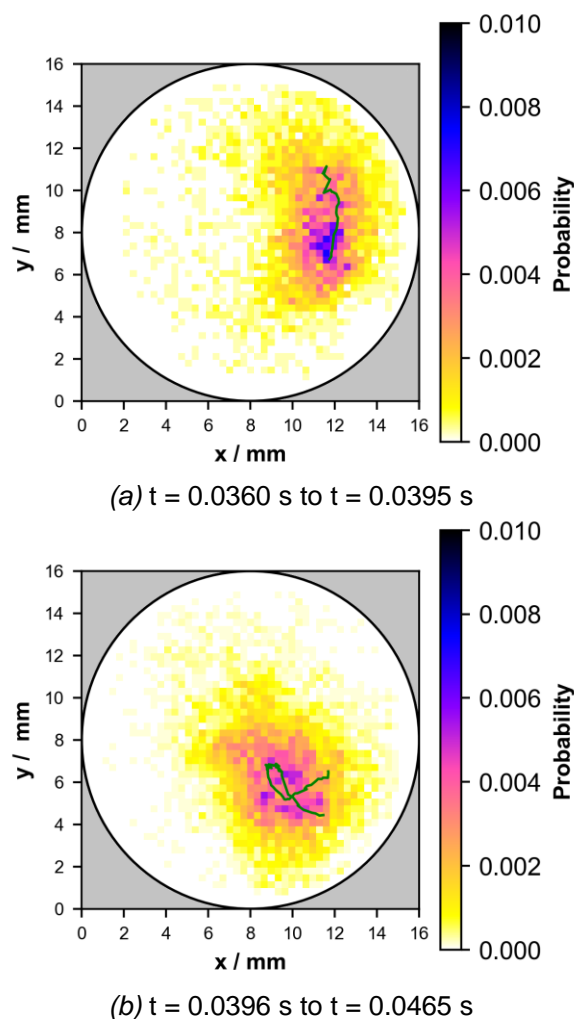


Figure 11. Two-dimensional joint probability distribution map of the tumble center locations between (a)  $t = 0.0360$  s and  $t = 0.0395$  s, and (b)  $t = 0.0396$  s and  $t = 0.0465$  s. The path followed by the tumble center in the mean shot is traced in green on both maps. For reference, the piston arrives at TDC at  $t = 0.0396$  s.

These observations provide insight into the flow processes occurring inside a large bore gas engine prechamber with key implications for the successful ignition of lean fuel-air mixtures and efficient operation of the engine. Furthermore, the salient features observed in the flow over the duration of the rapid compression stroke and the trends found also serve as targets for the development of

numerical simulations to model the flow. The successful implementation of time-resolved particle image velocimetry demonstrated in this study therefore establishes the foundation for further studies that will explore flow physics in prechambers.

#### 4 SUMMARY AND CONCLUSIONS

Detailed optical investigations have been performed to investigate the combustion process of ammonia and hydrogen. Schlieren imaging for laminar flame measurements and particle image velocimetry for flow field measurements have been applied on an optically accessible RCM. The following main results that concern the combustion characteristics of future fuels in large engines have been obtained.

##### Laminar flame measurements

- High-speed Schlieren images have been acquired of outwardly propagating spherical  $\text{NH}_3/\text{H}_2/\text{N}_2/\text{air}$  flames under quiescent conditions in the main chamber of a rapid compression machine.
- The evaluation range of flame radii for the laminar burning velocity is limited to  $r_f = 12$  mm on the RCM. For  $\text{NH}_3/\text{H}_2/\text{N}_2/\text{air}$  flames, a nonlinear extrapolation method to zero stretch is necessary. The onset of instabilities on the flame front prevents the determination of the laminar burning velocity under certain conditions.
- The LBV of  $\text{NH}_3/\text{H}_2/\text{N}_2/\text{air}$  flames decreases as the cracking ratio decreases and the pressure increases. From a peak LBV at slightly rich mixtures, the LBV decreases for leaner and richer mixtures. Under standard ambient temperature and pressure as well as quiescent conditions and stoichiometric mixtures, a cracking ratio of  $\gamma = 40\%$  is necessary to reach a LBV similar to that of  $\text{CH}_4$ .
- Despite a comparatively low evaluation range of flame radii, the present results correctly capture the effects of cracking ratio, equivalence ratio, and pressure on the LBV. The results for the LBV correspond well with the literature data for rich mixtures. For stoichiometric and lean mixtures, the stretch effect on the flame propagation cannot be fully captured. Therefore, the results for flames affected strongly by stretch, e.g.,  $\text{NH}_3/\text{H}_2/\text{N}_2/\text{air}$ , deviate from the literature data.

##### Flow field measurements

- Time-resolved planar two-component velocity fields inside a large engine prechamber

attached to a rapid compression machine have been acquired at a rate of 10 kHz.

- Velocity fields obtained show that a tumble vortex is formed consistently in the shots, but its motion in the field of view varies as it is subjected to stochastic flow fields.
- Inferred from a probability distribution of tumble center locations in the field of view, the variation in the path of the tumble center is seen to decrease after the piston reaches top dead center.

Combustion process development with future fuels like cracked  $\text{NH}_3$  must consider effects beyond the laminar conditions, namely instabilities and turbulence. The ratio of turbulent to laminar flame speed is severely different for  $\text{NH}_3$  and  $\text{CH}_4$  [9]. Therefore, future research will focus on capturing flow and turbulence conditions within large engines and studying the effects of instabilities and turbulence on flame propagation.

#### 5 DEFINITIONS, ACRONYMS, ABBREVIATIONS

**PIV:** Particle Image Velocimetry

**CFD:** Computational Fluid Dynamics

**PLIF:** Planar Laser-induced Fluorescence

**RCM:** Rapid Compression Machine

**BDC:** Bottom Dead Center

**TDC:** Top Dead Center

**LBV:** Laminar Burning Velocity

#### 6 ACKNOWLEDGMENTS

The authors would like to acknowledge the financial support of the "COMET - Competence Centers for Excellent Technologies" Program of the Austrian Federal Ministry for Climate Action, Environment, Energy, Mobility, Innovation and Technology (BMK) and the Austrian Federal Ministry of Labor and Economy (BMAW) and the Provinces of Salzburg, Styria and Tyrol for the COMET Centre (K1) LEC GETS. The COMET Program is managed by the Austrian Research Promotion Agency (FFG).

#### 7 REFERENCES AND BIBLIOGRAPHY

- [1] IPCC, "Climate Change 2022: Mitigation of Climate Change: Working Group III contribution to the Sixth Assessment Report of the Intergovernmental Panel on Climate Change," 2022.

- [2] The Royal Society, "Ammonia: zero-carbon fertiliser, fuel and energy store," London, U.K., 2020.
- [3] C. Garabedian and J. Johnson, "The theory of operation of an ammonia burning internal combustion engine," 1966.
- [4] G. E. Andrews and D. Bradley, "Determination of burning velocities: A critical review," *Combustion and Flame*, vol. 18, no. 1, pp. 133–153, 1972, doi: 10.1016/S0010-2180(72)80234-7.
- [5] M. Faghhi and Z. Chen, "The constant-volume propagating spherical flame method for laminar flame speed measurement," *Science Bulletin*, vol. 61, no. 16, pp. 1296–1310, 2016, doi: 10.1007/s11434-016-1143-6.
- [6] X. Chen *et al.*, "Flame front evolution and laminar flame parameter evaluation of buoyancy-affected ammonia/air flames," *International Journal of Hydrogen Energy*, vol. 46, no. 77, pp. 38504–38518, 2021, doi: 10.1016/j.ijhydene.2021.09.099.
- [7] A. Hayakawa, T. Goto, R. Mimoto, Y. Arakawa, T. Kudo, and H. Kobayashi, "Laminar burning velocity and Markstein length of ammonia/air premixed flames at various pressures," *Fuel*, vol. 159, pp. 98–106, 2015, doi: 10.1016/j.fuel.2015.06.070.
- [8] R. Kanoshima *et al.*, "Effects of initial mixture temperature and pressure on laminar burning velocity and Markstein length of ammonia/air premixed laminar flames," *Fuel*, vol. 310, p. 122149, 2022, doi: 10.1016/j.fuel.2021.122149.
- [9] C. Lhuillier, P. Brequigny, F. Contino, and C. Mounaïm-Rousselle, "Experimental investigation on ammonia combustion behavior in a spark-ignition engine by means of laminar and turbulent expanding flames," *Proceedings of the Combustion Institute*, vol. 38, no. 4, pp. 5859–5868, 2021, doi: 10.1016/j.proci.2020.08.058.
- [10] G. J. Gotama *et al.*, "Measurement of the laminar burning velocity and kinetics study of the importance of the hydrogen recovery mechanism of ammonia/hydrogen/air premixed flames," *Combustion and Flame*, vol. 236, p. 111753, 2022, doi: 10.1016/j.combustflame.2021.111753.
- [11] S. Mashruk, S. E. Zitouni, P. Brequigny, C. Mounaïm-Rousselle, and A. Valera-Medina, "Combustion performances of premixed ammonia/hydrogen/air laminar and swirling flames for a wide range of equivalence ratios," *International Journal of Hydrogen Energy*, 2022, doi: 10.1016/j.ijhydene.2022.09.165.
- [12] N. Wang *et al.*, "Laminar burning characteristics of ammonia/hydrogen/air mixtures with laser ignition," *International Journal of Hydrogen Energy*, vol. 46, no. 62, pp. 31879–31893, 2021, doi: 10.1016/j.ijhydene.2021.07.063.
- [13] C. Lhuillier, P. Brequigny, N. Lamoureux, F. Contino, and C. Mounaïm-Rousselle, "Experimental investigation on laminar burning velocities of ammonia/hydrogen/air mixtures at elevated temperatures," *Fuel*, vol. 263, p. 116653, 2020, doi: 10.1016/j.fuel.2019.116653.
- [14] J. H. Lee, J. H. Kim, J. H. Park, and O. C. Kwon, "Studies on properties of laminar premixed hydrogen-added ammonia/air flames for hydrogen production," *International Journal of Hydrogen Energy*, vol. 35, no. 3, pp. 1054–1064, 2010, doi: 10.1016/j.ijhydene.2009.11.071.
- [15] J. Li, H. Huang, N. Kobayashi, Z. He, and Y. Nagai, "Study on using hydrogen and ammonia as fuels: Combustion characteristics and NO<sub>x</sub> formation," *Int. J. Energy Res.*, vol. 38, no. 9, pp. 1214–1223, 2014, doi: 10.1002/er.3141.
- [16] A. Ichikawa, A. Hayakawa, Y. Kitagawa, K. D. Kunkuma Amila Somarathne, T. Kudo, and H. Kobayashi, "Laminar burning velocity and Markstein length of ammonia/hydrogen/air premixed flames at elevated pressures," *International Journal of Hydrogen Energy*, vol. 40, no. 30, pp. 9570–9578, 2015, doi: 10.1016/j.ijhydene.2015.04.024.
- [17] P. Kumar and T. R. Meyer, "Experimental and modeling study of chemical-kinetics mechanisms for H<sub>2</sub>-NH<sub>3</sub>-air mixtures in laminar premixed jet flames," *Fuel*, vol. 108, pp. 166–176, 2013, doi: 10.1016/j.fuel.2012.06.103.
- [18] K. P. Shrestha *et al.*, "An experimental and modeling study of ammonia with enriched oxygen content and ammonia/hydrogen laminar flame speed at elevated pressure and temperature," *Proceedings of the Combustion Institute*, vol. 38, no. 2, pp. 2163–2174, 2021, doi: 10.1016/j.proci.2020.06.197.
- [19] B. Mei, J. Zhang, X. Shi, Z. Xi, and Y. Li, "Enhancement of ammonia combustion with partial fuel cracking strategy: Laminar flame propagation and kinetic modeling investigation of NH<sub>3</sub>/H<sub>2</sub>/N<sub>2</sub>/air mixtures up to

- 10 atm,” *Combustion and Flame*, vol. 231, p. 111472, 2021, doi: 10.1016/j.combustflame.2021.111472.
- [20] C. Ji, Z. Wang, Du Wang, R. Hou, T. Zhang, and S. Wang, “Experimental and numerical study on premixed partially dissociated ammonia mixtures. Part I: Laminar burning velocity of NH<sub>3</sub>/H<sub>2</sub>/N<sub>2</sub>/air mixtures,” *International Journal of Hydrogen Energy*, vol. 47, no. 6, pp. 4171–4184, 2022, doi: 10.1016/j.ijhydene.2021.10.269.
- [21] X. Han, Z. Wang, Y. He, Y. Zhu, R. Lin, and A. A. Konnov, “Uniqueness and similarity in flame propagation of pre-dissociated NH<sub>3</sub> + air and NH<sub>3</sub> + H<sub>2</sub> + air mixtures: An experimental and modelling study,” *Fuel*, vol. 327, p. 125159, 2022, doi: 10.1016/j.fuel.2022.125159.
- [22] H. Lesmana, M. Zhu, Z. Zhang, J. Gao, J. Wu, and D. Zhang, “Experimental and kinetic modelling studies of laminar flame speed in mixtures of partially dissociated NH<sub>3</sub> in air,” *Fuel*, vol. 278, p. 118428, 2020, doi: 10.1016/j.fuel.2020.118428.
- [23] A. Goldmann and F. Dinkelacker, “Approximation of laminar flame characteristics on premixed ammonia/hydrogen/nitrogen/air mixtures at elevated temperatures and pressures,” *Fuel*, vol. 224, pp. 366–378, 2018, doi: 10.1016/j.fuel.2018.03.030.
- [24] O. Mathieu and E. L. Petersen, “Experimental and modeling study on the high-temperature oxidation of Ammonia and related NO<sub>x</sub> chemistry,” *Combustion and Flame*, vol. 162, no. 3, pp. 554–570, 2015, doi: 10.1016/j.combustflame.2014.08.022.
- [25] M. Comotti and S. Frigo, “Hydrogen generation system for ammonia–hydrogen fuelled internal combustion engines,” *International Journal of Hydrogen Energy*, vol. 40, no. 33, pp. 10673–10686, 2015, doi: 10.1016/j.ijhydene.2015.06.080.
- [26] C. Lhuillier, P. Brequigny, F. Contino, and C. Mounaïm-Rousselle, “Experimental study on ammonia/hydrogen/air combustion in spark ignition engine conditions,” *Fuel*, vol. 269, p. 117448, 2020, doi: 10.1016/j.fuel.2020.117448.
- [27] C. S. Mørch, A. Bjerre, M. P. Gøttrup, S. C. Sorenson, and J. Schramm, “Ammonia/hydrogen mixtures in an SI-engine: Engine performance and analysis of a proposed fuel system,” *Fuel*, vol. 90, no. 2, pp. 854–864, 2011, doi: 10.1016/j.fuel.2010.09.042.
- [28] C. Mounaïm-Rousselle, P. Bréquigny, C. Dumand, and S. Houillé, “Operating Limits for Ammonia Fuel Spark-Ignition Engine,” *Energies*, vol. 14, no. 14, p. 4141, 2021, doi: 10.3390/en14144141.
- [29] F. R. Westlye, A. Ivarsson, and J. Schramm, “Experimental investigation of nitrogen based emissions from an ammonia fueled SI-engine,” *Fuel*, vol. 111, pp. 239–247, 2013, doi: 10.1016/j.fuel.2013.03.055.
- [30] A. N. Lipatnikov and J. Chomiak, “Molecular transport effects on turbulent flame propagation and structure,” *Progress in Energy and Combustion Science*, vol. 31, no. 1, pp. 1–73, 2005, doi: 10.1016/j.pecs.2004.07.001.
- [31] P. Brequigny, F. Halter, and C. Mounaïm-Rousselle, “Lewis number and Markstein length effects on turbulent expanding flames in a spherical vessel,” *Experimental Thermal and Fluid Science*, vol. 73, pp. 33–41, 2016, doi: 10.1016/j.expthermflusci.2015.08.021.
- [32] M. Kotzagianni, P. Kyrtatos, and K. Boulouchos, “Optical investigation of prechamber combustion in an RCEM,” *Combustion Engines*, 176(1), pp. 10–15, 2019.
- [33] R. Wellander *et al.*, “Study of the Early Flame Development in a Spark-Ignited Lean Burn Four-Stroke Large Bore Gas Engine by Fuel Tracer PLIF,” *SAE Int. J. Engines*, vol. 7, no. 2, pp. 928–936, 2014, doi: 10.4271/2014-01-1330.
- [34] E. Mastorakos *et al.*, “Fundamental Aspects of Jet Ignition for Natural Gas Engines,” *SAE Int. J. Engines*, vol. 10, no. 5, pp. 2429–2438, 2017, doi: 10.4271/2017-24-0097.
- [35] P. M. Allison, M. de Oliveira, A. Giusti, and E. Mastorakos, “Pre-chamber ignition mechanism: Experiments and simulations on turbulent jet flame structure,” *Fuel*, vol. 230, pp. 274–281, 2018, doi: 10.1016/j.fuel.2018.05.005.
- [36] F. Liyan *et al.*, “Research on the Characteristics of Enrichment Fuel Injection Process in the Pre-Chamber of a Marine Gas Engine,” in *SAE Technical Paper Series*, 2015.
- [37] C. Kiesling *et al.*, “Experimental Investigation of the Influence of Ignition System Parameters on Combustion in a Rapid Compression-Expansion Machine,” in *SAE Technical Paper Series*, 2020.
- [38] Z. Chen, “On the accuracy of laminar flame speeds measured from outwardly

- propagating spherical flames: Methane/air at normal temperature and pressure,” *Combustion and Flame*, vol. 162, no. 6, pp. 2442–2453, 2015, doi: 10.1016/j.combustflame.2015.02.012.
- [39] M. P. Burke, Z. Chen, Y. Ju, and F. L. Dryer, “Effect of cylindrical confinement on the determination of laminar flame speeds using outwardly propagating flames,” *Combustion and Flame*, vol. 156, no. 4, pp. 771–779, 2009, doi: 10.1016/j.combustflame.2009.01.013.
- [40] A. Tilz, G. Meyer, C. Kiesling, G. Pirker, S. Salbrechter, and A. Wimmer, “Design of a test rig for fundamental investigations of spark characteristics,” *International Journal of Engine Research*, vol. 21, no. 8, pp. 1412–1425, 2020, doi: 10.1177/1468087419828943.
- [41] A. P. Kelley and C. K. Law, “Nonlinear effects in the extraction of laminar flame speeds from expanding spherical flames,” *Combustion and Flame*, vol. 156, no. 9, pp. 1844–1851, 2009, doi: 10.1016/j.combustflame.2009.04.004.
- [42] P. D. Ronney and G. I. Sivashinsky, “A Theoretical Study of Propagation and Extinction of Nonsteady Spherical Flame Fronts,” *SIAM Journal on Applied Mathematics*, vol. 49, no. 4, pp. 1029–1046, 1989. [Online]. Available: <http://www.jstor.org/stable/2102004>
- [43] Z. Chen, M. P. Burke, and Y. Ju, “Effects of Lewis number and ignition energy on the determination of laminar flame speed using propagating spherical flames,” *Proceedings of the Combustion Institute*, vol. 32, no. 1, pp. 1253–1260, 2009, doi: 10.1016/j.proci.2008.05.060.
- [44] D. G. Goodwin, R. L. Speth, H. K. Moffat, and B. W. Weber, *Cantera: An Object-oriented Software Toolkit for Chemical Kinetics, Thermodynamics, and Transport Processes*: Zenodo, 2021.
- [45] A. A. Konnov, “Implementation of the NCN pathway of prompt-NO formation in the detailed reaction mechanism,” *Combustion and Flame*, vol. 156, no. 11, pp. 2093–2105, 2009, doi: 10.1016/j.combustflame.2009.03.016.
- [46] Alex Liberzon, Theo Käufer, Andreas Bauer, Peter Vennemann, and Erich Zimmer, *OpenPIV/openpiv-python: OpenPIV-Python v0.23.6*: Zenodo, 2021.
- [47] D. Garcia, “A fast all-in-one method for automated post-processing of PIV data,” *Exp Fluids*, vol. 50, no. 5, pp. 1247–1259, 2011, doi: 10.1007/s00348-010-0985-y.
- [48] J. K. Bechtold and M. Matalon, “Hydrodynamic and diffusion effects on the stability of spherically expanding flames,” *Combustion and Flame*, vol. 67, no. 1, pp. 77–90, 1987, doi: 10.1016/0010-2180(87)90015-0.
- [49] G. E. Andrews and D. Bradley, “The burning velocity of methane-air mixtures,” *Combustion and Flame*, vol. 19, no. 2, pp. 275–288, 1972, doi: 10.1016/S0010-2180(72)80218-9.
- [50] T. Wang, W. Li, M. Jia, D. Liu, W. Qin, and X. Zhang, “Large-eddy simulation of in-cylinder flow in a DISI engine with charge motion control valve: Proper orthogonal decomposition analysis and cyclic variation,” *Applied Thermal Engineering*, vol. 75, pp. 561–574, 2015, doi: 10.1016/j.applthermaleng.2014.10.081.
- [51] J. Rabault, J. A. Vernet, B. Lindgren, and P. H. Alfredsson, “A study using PIV of the intake flow in a diesel engine cylinder,” *International Journal of Heat and Fluid Flow*, vol. 62, pp. 56–67, 2016, doi: 10.1016/j.ijheatfluidflow.2016.06.020.
- [52] M. Bunce, A. Cairns, S. Krishna Pothuraju Subramanyam, N. Peters, and H. Blaxill, “The Influence of Charge Motion on Pre-Chamber and Main Chamber Combustion in a Highly Dilute Jet Ignition Engine,” *Front. Mech. Eng.*, vol. 6, 2021, doi: 10.3389/fmech.2020.629243.
- [53] L. Graftieaux, M. Michard, and N. Grosjean, “Combining PIV, POD and vortex identification algorithms for the study of unsteady turbulent swirling flows,” *Meas. Sci. Technol.*, vol. 12, no. 9, pp. 1422–1429, 2001, doi: 10.1088/0957-0233/12/9/307.
- [54] A. Kirkpatrick, G.-H. Kim, and D. Olsen, “CFD Modeling of the Performance of a Prechamber for Use in a Large Bore Natural Gas Engine,” in *ASME 2005 Internal Combustion Engine Division Spring Technical Conference*, Chicago, Illinois, USA, 2005, pp. 397–403.